

k -resolved susceptibility function of $2H$ -TaSe₂ from angle-resolved photoemission

J. Laverock,¹ D. Newby, Jr.,¹ E. Abreu,¹ R. Averitt,¹ K. E. Smith,¹
R. P. Singh*,² G. Balakrishnan,² J. Adell,³ and T. Balasubramanian³

¹*Department of Physics, Boston University, 590 Commonwealth Avenue, Boston, Massachusetts 02215, USA*

²*Department of Physics, University of Warwick, Coventry, CV4 7AL, United Kingdom*

³*MAX-lab, Lund University, SE-221 00 Lund, Sweden*

The connection between the Fermi surface and charge-density wave (CDW) order is revisited in $2H$ -TaSe₂. Using angle-resolved photoemission spectroscopy, *ab initio* band structure calculations, and an accurate tight-binding model, we develop the *empirical* k -resolved susceptibility function, which we use to highlight states that contribute to the susceptibility for a particular \mathbf{q} -vector. We show that although the Fermi surface is involved in the peaks in the susceptibility associated with CDW order, it is *not* through conventional Fermi surface nesting, but rather through finite energy transitions from states located far from the Fermi level. Comparison with monolayer TaSe₂ illustrates the different mechanisms that are involved in the absence of bilayer splitting.

I. INTRODUCTION

The question of whether nesting instabilities of the Fermi surface (FS) can drive charge density wave (CDW) formation in real materials has been the topic of numerous experimental and theoretical investigations for many years.¹⁻³ In cases of apparently well-nested FSs, subsequent inspection of the real part of the generalized susceptibility, which is the relevant quantity in assessing instabilities in the electronic system, and its imaginary counterpart (which is not) can rule against FS nesting being the *primary* driving force.⁴ In concert with instabilities in the electronic system, lattice effects (through the softening of phonon modes associated with the CDW) must also be considered on an equal footing.⁵

The analysis of the electronic susceptibility of a material is central in determining whether an electronic instability that may be due to FS nesting is capable of driving some associated ordering phenomena. Typically, the \mathbf{q} landscape of the real and imaginary parts of the susceptibility are compared, and a peak that survives in both parts is taken as evidence that FS nesting may play a role in emergent phenomena that occurs at that wavevector. However, the susceptibility function represents an integral over the Brillouin zone (BZ), i.e. over all \mathbf{k} -states. Consequently, one of the deficiencies of this approach is that some of the most important information that is available in the susceptibility is integrated out; That is to say, *which* electrons actually contribute to the instability. In order to illustrate the importance of the \mathbf{k} -dependence of the susceptibility, we introduce it here on a prototypical system, $2H$ -TaSe₂, and demonstrate, from an experimental perspective, the additional insight that is available from this kind of analysis.

Of the many CDW materials, the transition metal dichalcogenides are amongst the most well-known and

well-studied.^{1,6} Indeed, it is surprising that after the many experimental⁷⁻¹³ and theoretical^{4,14-17} investigations, $2H$ -TaSe₂ still courts controversy as to whether the FS is responsible for its CDW. Below $T_0 = 122$ K, an incommensurate CDW transition with a wave vector $\mathbf{q} = (1 - \delta)\frac{2}{3}\Gamma M$ develops, with $\delta \sim 0.02$, which experiences a lock-in to a commensurate structure ($\delta = 0$) below 90 K.¹⁸ The isoelectronic and isostructural compound $2H$ -NbSe₂, also hosts a similar incommensurate CDW at $T_0 = 33.5$ K.¹⁸ Experimentally, the topology of the FS of TaSe₂ and NbSe₂ are quantitatively different,¹⁰⁻¹² which immediately raises difficulties with the conventional FS nesting model. In particular, state-of-the-art bandstructure results firmly rule out the FS nesting model,⁴ whereas some recent high-resolution angle-resolved photoemission (ARPES) measurements contradict the theory, suggesting a primary role for the FS via its experimental autocorrelation map.^{13,19}

Here, we address this controversy directly through complementary ARPES measurements and *ab initio* bandstructure calculations. Through careful band and \mathbf{k} -resolved calculations of the experimental susceptibility, at energies near and far away from the Fermi level (E_F), we show that FS nesting is too weak to drive CDW order. Instead, peaks in the susceptibility that are often associated with the CDW originate through finite energy transitions from bands nested away from E_F . We show that this concept explains both the temperature dependent ARPES spectral function,^{13,19} as well as why the material has courted controversy for so long. Although FS nesting can be ruled out, the Fermi wave vector, \mathbf{k}_F does play a role, both directly and (more importantly) indirectly, in determining the peaks in the susceptibility. We suggest that similar careful inspection of the \mathbf{k} -resolved susceptibility function in other materials will be capable of discriminating between different models of charge, spin or superconducting order.

*Present address: Department of Physics, IISER Bhopal, MP-462023, India

II. ELECTRONIC STRUCTURE

Ab initio calculations

The electronic structure has been calculated for $2H$ -TaSe₂ using the full-potential linear augmented plane-wave (FLAPW) ELK code within the local density approximation (LDA),²⁰ including spin-orbit coupling self-consistently, and using the experimental structural parameters.²¹ Relaxation of the unit cell was not found to significantly affect the band structure, particularly near E_F . The band structure of TaSe₂ is shown in Fig. 1(a), and is in close agreement with previous electronic structure calculations.^{4,17} Two Ta d bands, split by the double TaSe₂ layer, cross E_F and form the FS shown on the left of Fig. 1(b). A slight shift downwards in E_F by ~ 50 meV, recovers the more familiar FS that has previously been suggested by experiment.^{12,13,19} This shifted FS, shown on the right side of Fig. 1(b), is topologically similar to experiment, and consists of Γ - and K -centered hole “barrel” sheets, from the first band, and M -centered electron “dogbone” sheets from the second. In the following, we refer to the topology of this more familiar, shifted FS. Note that the downwards shift in E_F leads to a reduction in the band filling of these sheets to 1.80 electrons (from 2). As pointed out by Refs. 4,22, relativistic effects are not negligible for the heavy Ta ion. Through time-reversal symmetry,²³ the scalar relativistic bands are degenerate across the entire top face ($ALHA$) of the BZ. However, with the inclusion of relativistic effects (in the form of spin-orbit coupling) this restriction is lifted, and the degeneracy is broken. This has important, and non-trivial, effects on the FS, allowing the barrel and dogbone FS sheets to be fully disconnected everywhere (except along AL) in the zone, which ultimately leads to a much more 2D dogbone FS (which, in turn, ought to enhance the propensity for nesting).

Tight-binding model

In order to parameterize the experimental $E(\mathbf{k})$ relation, a simple 2D tight-binding (TB) model is constructed:

$$E_j(\mathbf{k}) = E_{0,j} + \sum_{\mathbf{R}} t_{|\mathbf{R}|,j} \cos(\mathbf{k} \cdot \mathbf{R}), \quad (1)$$

where \mathbf{R} are the hexagonal 2D lattice vectors $\mathbf{a} = (\sqrt{3}a/2, \pm a/2)$, $t_{|\mathbf{R}|}$ are the TB hopping parameters and j is the band index of the two bands that form the FS (E_0 is an energy offset).¹⁵ In this model, a total of 15 nearest-neighbors were required to satisfactorily describe a constant k_z slice of the LDA band structure. Note that a large number of $t_{|\mathbf{R}|}$ are used in this work in order to accurately describe both the theoretical and experimental $E(\mathbf{k})$, and we attach no specific meaning to the individual parameters. Before fitting the TB model

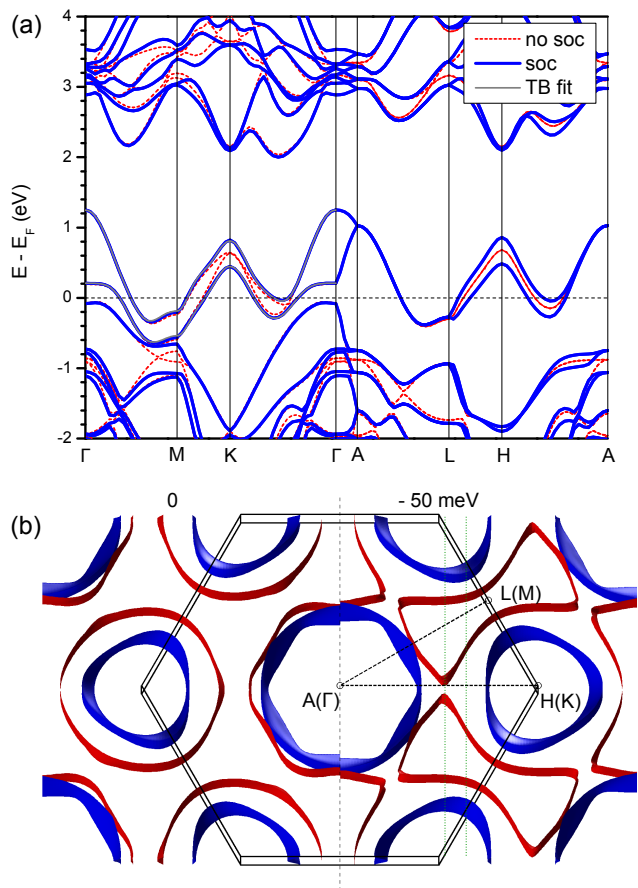


FIG. 1: (Color online) (a) LDA band structure of $2H$ -TaSe₂ including, and neglecting, spin-orbit coupling (soc). The TB_{LDA} model is shown through $k_z = 0$ in gray. (b) The FS of $2H$ -TaSe₂, including soc. The left part shows the raw LDA FS, and in the right E_F has been shifted by -50 meV. Symmetry points in brackets indicate those at $k_z = 0$. The vertical dotted lines are the slices used in Fig. 4(c).

to the experimental data, we first check its suitability by assessing how well it is able to describe the theoretical LDA band structure. The results of fitting the TB model to the $k_z = 0$ plane of the LDA band structure (TB_{LDA}), shown in Fig. 1(a), agree with the LDA result to within 5 meV r.m.s. in energy. These TB_{LDA} parameters are only used here to illustrate the capability of the 15-term TB model in fully capturing the band dispersion of TaSe₂, and its excellent agreement with the *ab initio* result demonstrates the anticipated accuracy of the model in describing the *experimental* dispersion relation. For the remainder of the text, the TB_{LDA} parameters are discarded. Below, we instead carefully fit the experimental data to the TB model, yielding TB_{exp} , which we use for all subsequent analysis. Although the model does not explicitly include spin-orbit coupling, the non-degeneracy of the parameters of the two bands allow for its effects to be fully captured implicitly.

Angle-resolved photoemission measurements

Single-crystals of $2H\text{-TaSe}_2$ were grown by the chemical vapor transport technique using iodine as the transport agent.^{21,24} Samples were cleaved in ultra-high vacuum and oriented with reference to low-energy electron diffraction patterns. Angle-resolved photoemission measurements were performed at Beamline I4, MAX-lab, Lund University, Sweden at 100 K with a photon energy of 50 eV and total instrument resolution of 9 meV. At this temperature, TaSe_2 is in the incommensurate CDW phase, and experiences almost no change in its electronic structure compared with the normal state.^{9,13} The Fermi level was referenced to a gold foil in electrical contact with the sample. The experimental dispersion relation near E_F is determined through the 2D curvature of the constant-energy ARPES intensity map,²⁵ $I = I(p_x, p_y)$:

$$C(p_x, p_y) = \frac{(a_0 + I_x^2)I_{yy} - 2I_x I_y I_{xy} + (a_0 + I_y^2)I_{xx}}{2(a_0 + I_x^2 + I_y^2)^{\frac{3}{2}}}, \quad (2)$$

where $I_x = \partial I / \partial p_x$, $I_{xx} = \partial^2 I / \partial p_x^2$ and $I_{xy} = \partial^2 I / \partial p_x \partial p_y$ are the partial derivatives of I , and a_0 is an arbitrary constant, optimized to maximize the contrast of $C(p_x, p_y)$. Analysis of the extrema of this function has recently been shown to accurately locate both band dispersions and FS crossings in ARPES measurements.²⁵ Here, we find it provides significantly enhanced contrast compared to analysis of the first and/or second derivatives by themselves, as well as being capable of capturing dispersion parallel to either direction.

The TB model has been fitted²⁶ to the detected loci to provide a parameterized description of the experimental $E(\mathbf{k})$ for $E \leq E_F$, which we refer to as TB_{exp} .²⁷ The energy range of the fit is restricted to -260 meV to $+40$ meV in order to avoid including the flat portions of the bottom of the bands in the fit; note that these states are still included in the subsequent analysis. Experimentally, the bottom of the lower Ta d band is found to be -340 meV, and so most of the band dispersion is included. In addition to the TB amplitudes, $t_{|\mathbf{R}|,j}$, and offsets, $E_{0,j}$, four other adjustable parameters are varied in the fit, including the lattice parameter, origin in p_x and p_y (projected Γ -point), and azimuthal alignment, θ .

The results of the fitted TB_{exp} model are shown in Fig. 2 alongside the ARPES spectra and the shifted LDA result (recall that the raw calculation yields a topologically different FS). The fit is in excellent agreement with the data, in both constant energy slices [shown near E_F in Fig. 2(a)] and constant momentum slices [an example is shown in Fig. 2(b)]. The occupied area of the TB model is 1.92, which is in closer agreement with the nominal electron count of 2 than the shifted LDA calculation. This quantity is based on a 2D cut through the 3D band structure, and is therefore not restricted to obey the Luttinger electron count, but nevertheless, it is satisfyingly close. The FS of the TB_{exp} model is close to previous ARPES measurements,^{12,13,19} although the Γ and K barrels of

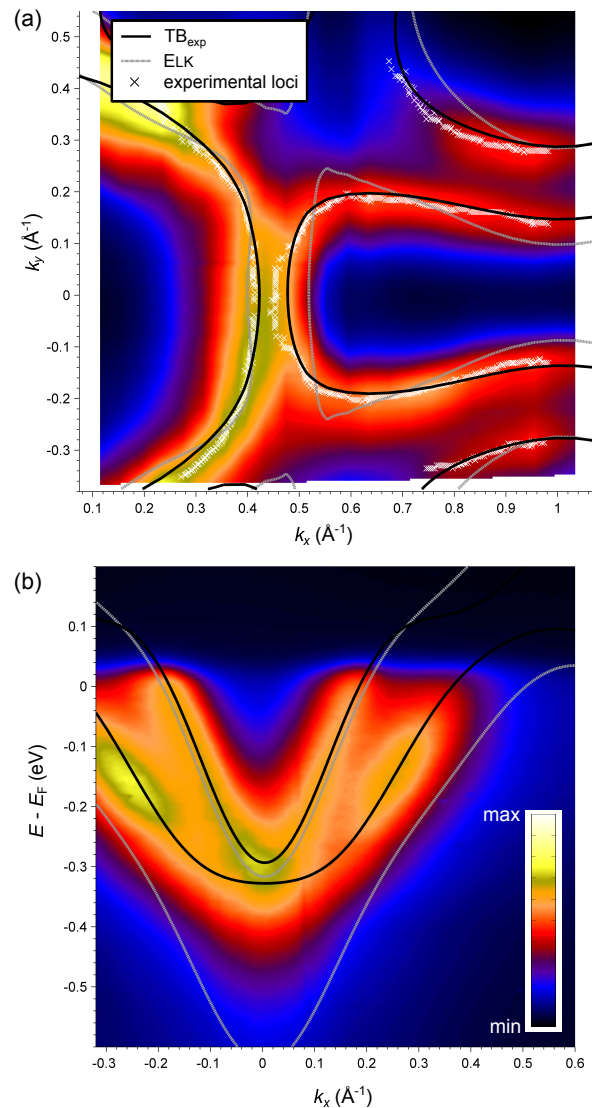


FIG. 2: (Color online) (a) ARPES intensity map at E_F compared with the FS of the shifted (by -50 meV) LDA calculation (light dashed lines) and of the TB fit to the data (dark solid lines). The detected band loci are also shown as white crosses. (b) Energy-momentum cut through $k_x = 0.754 \text{ \AA}^{-1}$.

our FS are slightly smaller and larger respectively than Refs. 13,19. Since this discrepancy cannot be reproduced by shifts in E_F , (these sheets are of the same band), it may reflect a slightly different k_{\perp} associated with the two different measurements. Nevertheless, the following analysis of the data is not affected by changes in \mathbf{k}_F of these sheets, lending more weight to the argument that FS nesting is weak in TaSe_2 .

III. NONINTERACTING SUSCEPTIBILITY

Ab initio susceptibility

The role of nesting in the LDA has been theoretically investigated via calculations of the noninteracting susceptibility,

$$\chi_0(\mathbf{q}, \omega) = \sum_{\mathbf{k}} \frac{f(\epsilon_{\mathbf{k}}) - f(\epsilon_{\mathbf{k}+\mathbf{q}})}{\epsilon_{\mathbf{k}} - \epsilon_{\mathbf{k}+\mathbf{q}} - \omega - i\delta}, \quad (3)$$

for wave vector \mathbf{q} and frequency $\omega \rightarrow 0$, in which $f(\epsilon_{\mathbf{k}})$ is the Fermi occupancy of state $\epsilon_{\mathbf{k}}$.^{4,28} The imaginary part ($\text{Im} \chi_0$), which gathers transitions in a narrow window of energies near the FS and can be directly associated with FS nesting, is shown for TaSe₂ in Fig. 3(a) and exhibits some weak peaks close to, but offset from, \mathbf{q}_{CDW} . The most overwhelming feature is not at this wavevector, however, but at $q = K$, in which dogbone nesting dominates. $\text{Im} \chi_0$, whilst indicating FS nesting, is not responsible for CDW order, which instead depends on the real part, $\text{Re} \chi_0$. $\text{Re} \chi_0$ involves transitions over a bandwidth-size window of energies, and for TaSe₂ is dominated by interband transitions between the two Ta *d* bands. The intensity at K is completely suppressed, and instead $\text{Re} \chi_0$ peaks at \mathbf{q}_{CDW} , reflecting the electronic instability that eventually develops into the CDW. These results, and their interpretation, are very similar to previous LDA calculations of $\chi_0(\mathbf{q}, \omega)$ of TaSe₂ and NbSe₂.^{4,29} As we will show below, from both an experimental *and* theoretical perspective, this peak in $\text{Re} \chi_0$ has little to do with conventional FS nesting, and is rather associated with ‘nesting’ between the two bands over energies far from E_F .

Tight-binding susceptibility

In Fig. 3(b), the noninteracting susceptibility, $\chi_{0,\text{tb}}(\mathbf{q}, \omega)$, of the experimental tight-binding model, TB_{exp} , is shown along the same path as the *ab initio* result. This susceptibility, calculated from the experimental band structure, represents an accurate reflection of the *experimental* susceptibility function. Here, a temperature of 8 meV is used to fill the states (comparable with the experiment), although in practice this has little influence on the overall structure of the susceptibility. This result, which is based on a 2D slice of the electronic structure, is of course cruder than the full 3D calculation shown in Fig. 3(a); nevertheless, the two results are very similar to one another. In $\text{Re} \chi_{0,\text{tb}}$, the function exhibits a peak near \mathbf{q}_{CDW} , which is predominantly due to interband transitions. However, the wave vector of this feature is somewhat offset from \mathbf{q}_{CDW} , rather developing at $\mathbf{q}^* = 0.56 \Gamma M$. Correspondingly, although $\text{Im} \chi_{0,\text{tb}}$ exhibits a weak peak at \mathbf{q}^* it is neither very intense nor significantly stronger than other local peaks elsewhere in

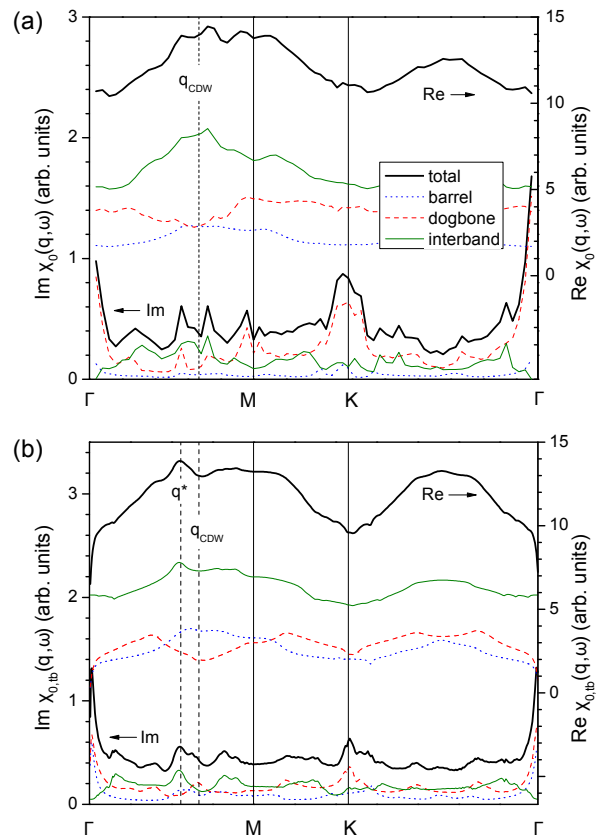


FIG. 3: (Color online) Real and imaginary parts of the non-interacting susceptibility, $\chi_0(\mathbf{q}, \omega)$, for (a) the 3D *ab initio* ELK band structure, and (b) the 2D TB_{exp} model bands. The commensurate CDW wave vector, $\mathbf{q}_{\text{CDW}} = 2/3 \Gamma M$ is indicated by the dashed line, and $\mathbf{q}^* = 0.56 \Gamma M$ indicates the maximum in the TB_{exp} susceptibility. Note that the real axis is vertically offset for clarity.

the BZ, for example at $\mathbf{q} = K$, despite the reduced dimensionality of this 2D model. In fact, this suppression of the susceptibility peak is observed in other ARPES models,^{12,19} which consistently suggest a slightly lower \mathbf{q} ($\sim 0.6 \Gamma M$) than the CDW wave vector. This suggests that ultimately, electron-phonon coupling likely decides which wave vector is chosen for the ordering.^{5,30} In all models investigated here, the susceptibility peak is relatively broad and is certainly compatible with the CDW wave vector.

\mathbf{k} -resolved susceptibility

Unlike typical calculations of the electronic susceptibility, we now explicitly resolve the \mathbf{k} dependence of the susceptibility function, enabling us to directly assess *which* states contribute to $\chi_{0,\text{tb}}(\mathbf{q}, \omega)$:

$$\chi_{0,\text{tb}}(\mathbf{q}, \mathbf{k}) = \frac{f(\epsilon_{\mathbf{k}}) - f(\epsilon_{\mathbf{k}+\mathbf{q}})}{\epsilon_{\mathbf{k}} - \epsilon_{\mathbf{k}+\mathbf{q}} - \omega - i\delta}. \quad (4)$$

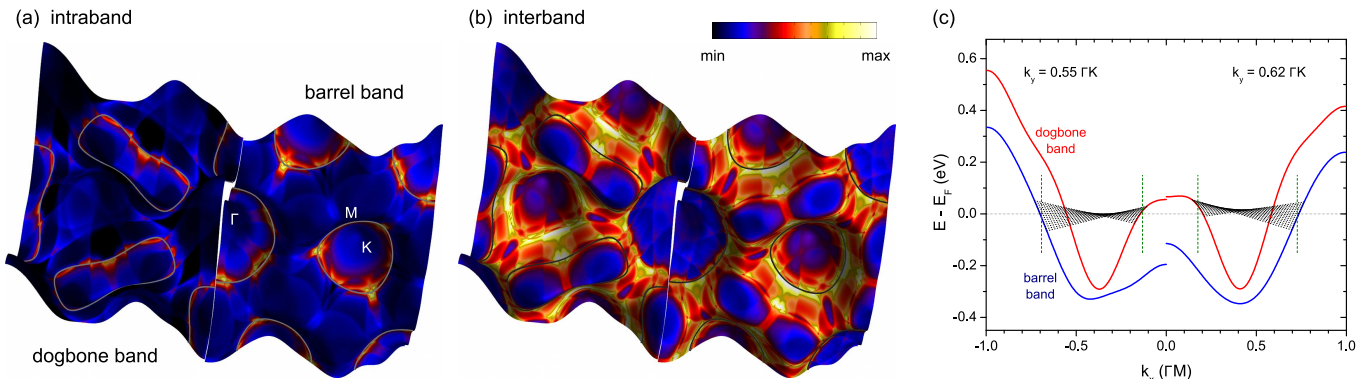


FIG. 4: (Color online) Real part of the \mathbf{k} -resolved susceptibility function of the TB_{exp} model for $\mathbf{q} = \mathbf{q}^*$, showing (a) intraband (dogbone \rightarrow dogbone and barrel \rightarrow barrel) transitions, and (b) interband (dogbone \leftrightarrow barrel) transitions. The height of the surface is the TB_{exp} band energy, whereas the color [the same color scale is used in both (a) and (b)] denotes the magnitude of the \mathbf{k} -resolved susceptibility. The FS of each band is shown by the gray lines. (c) Slice of the TB_{exp} bands through the vertical lines of Fig. 1(b). The dotted lines all have the same length of \mathbf{q}^* . Vertical dashed lines indicate the maxima of the \mathbf{k} -resolved susceptibility for this slice.

Here, the integral over the BZ has been dropped with respect to Eq. 3. For a given value of \mathbf{q} , this function separates the contribution of each individual \mathbf{k} -point to the susceptibility, allowing the direct visualization in \mathbf{k} -space of which states are connected by that particular wave vector. For example, for conventional FS nesting this function will have high intensity only in a narrow region of \mathbf{k} -space near the FS, and will be weak elsewhere. Integration of this function over \mathbf{k} recovers the usual susceptibility function [i.e. that shown in Fig. 3(b)].

In Figs. 4(a,b), $\text{Re } \chi_{0,\text{tb}}(\mathbf{q}^*, \mathbf{k})$ is shown of the experimental TB model (TB_{exp}) for $\mathbf{q} = \mathbf{q}^*$. Here, the magnitude of $\text{Re } \chi_{0,\text{tb}}(\mathbf{q}^*, \mathbf{k})$ is shown as a color intensity on top of the energy surface of the TB_{exp} bands. In this presentation, ‘hotspots’ indicate states that are connected to other states of different occupancy by the wave vector \mathbf{q}^* , and their intensity reflects their proximity in energy. For reference, the TB_{exp} FS is also shown in Figs. 4(a,b) as gray contours.

The intraband contributions [Fig. 4(a)] of both dogbone (left) and barrel (right) bands are weak, and only supply intensity near their respective FSs. It is noted that even though this function has intensity only near the two FSs, the structure is ‘smeared’ over a relatively large energy range. Overall, states at least 80 meV away from E_F contribute significantly to the intraband $\chi_{0,\text{tb}}(\mathbf{q}, \omega)$, which is not compatible with the conventional FS nesting model. On the other hand, the interband transitions [Fig. 4(b)] show strong intensity over the entire \mathbf{k} range of the bands between the two FSs, irrespective of their energies (which differ by as much as 300 meV in this part of \mathbf{k} -space). This part of the BZ is precisely that in which the two bands have different occupancies, and therefore in which transitions are available (through the numerator of Eq. 3). Similar results are obtained near \mathbf{q}^* (including at \mathbf{q}_{CDW}) from the *ab initio* unshifted LDA results, despite the different FS topology, as well as from other TB parameterizations of the energy bands.¹⁹ The involve-

ment of such a large region of \mathbf{k} -space in contributing to the susceptibility function, at its peak in \mathbf{q} , is compelling and direct *experimental* evidence against conventional FS nesting.

IV. DISCUSSION

Despite our conclusion that FS nesting is not relevant in deciding the peak in the susceptibility of $2H\text{-TaSe}_2$, it is evident from Fig. 4(b) that there is a reasonable contribution from interband transitions near the FS, and it is prudent to ask why this is, given that both $\text{Im } \chi_{0,\text{tb}}$ and the *ab initio* $\text{Im } \chi_0$ clearly rule FS nesting out. In Fig. 4(c), two slices of the TB_{exp} energy bands through $k_y = 0.55 \Gamma K$ and $k_y = 0.62 \Gamma K$ are shown, corresponding to a vertical slice in Fig. 1(b) through both the K barrels and dogbones. The dotted lines in Fig. 4(c) all have the same length in \mathbf{k} -space, *viz.* \mathbf{q}^* , and connect unoccupied barrel band states to occupied dogbone band states and *vice versa*. These transitions give rise to the hotspots in Fig. 4(b) between the K barrel FS and dogbone FS as well as at the saddle point along ΓK . The most intense features in $\text{Re } \chi_{0,\text{tb}}$ are shown by vertical dotted lines, and lie in close proximity to the indicated transitions. Whilst a transition *at* the FS is present, particularly for $k_y = 0.55 \Gamma K$, there is a large number of finite energy transitions at the same wave vector. The similar magnitude, but opposite, Fermi velocities of the two bands ensure that this is true over a large energy range. For $k_y = 0.62 \Gamma K$, the \mathbf{q}^* vector does not connect to pieces of FS, and instead the FS of each band is connected to a finite energy *away* from the FS of the other band. This explains why intensity at the FS is visible in Fig. 4(b), but very weak in $\text{Im } \chi_{0,\text{tb}}$. Although some transitions are available at the FS, there are many more at finite energy which overwhelm the low-energy transitions. This concept has similarities, although is more

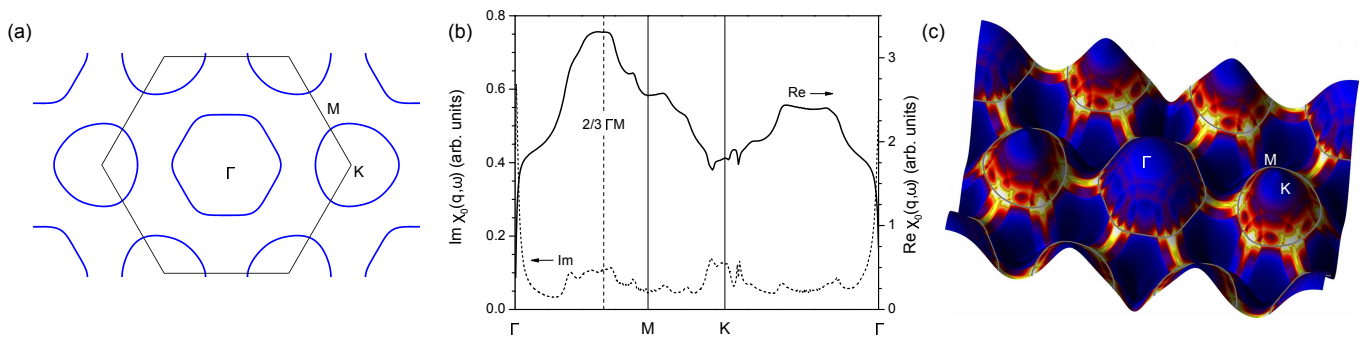


FIG. 5: (Color online) Electronic structure and susceptibility of monolayer $2H$ -TaSe₂: (a) Fermi surface, (b) noninteracting susceptibility, $\chi_0(\mathbf{q}, \omega)$, and (c) real part of the \mathbf{k} -resolved susceptibility for $\mathbf{q} = \frac{2}{3} \Gamma M$.

general, to the idea of “hidden nesting”,³ and has been used to explain finite energy transitions in 1D materials in which FS nesting is ‘hidden’ by band hybridization effects. We note that although this explanation was mentioned by Ref. 4, who also categorically ruled out FS nesting, reports of FS nesting-driven CDW order in the dichalcogenides still pervade the literature.

This explanation of the susceptibility also provides a natural explanation for why the FS has been implicated in previous studies. To illustrate this, we consider two bands that have equal and opposite velocities near E_F , similar to the case for TaSe₂ in Fig. 4(c), and which can be idealized in one dimension as two linear bands of slope $\pm a$ and with Fermi crossings separated by $k_2 - k_1$. As demonstrated by Johannes *et al.*, $\chi(\mathbf{q})$ can be expanded via $\chi(\mathbf{q}) = \int_{-\infty}^{E_F} dx \int_{E_F}^{\infty} dy F(x, y)/(x - y)$, where $F(x, y) = \int \delta(\epsilon_{\mathbf{k}} - x) \delta(\epsilon_{\mathbf{k}+\mathbf{q}} - y) d\mathbf{k}$.²⁹ The variables x and y relate to states below and above E_F . In the idealized 1D model, contributions to $\chi(q)$ are satisfied for $q = (x + y)/a + (k_2 - k_1)$, and are weighted by the energy separation, $x - y$. The integrals over x and y , however, are symmetric about E_F , and this function must peak at $q = (k_2 - k_1)$, regardless of whether states near E_F contribute or not. Over the full energy window, corresponding to $\text{Re} \chi(q)$, the function peaks at this wave vector, not due to FS transitions but rather due to finite energy transitions (or deep energy nesting). More generally, in 2D systems this effect is spread out by dispersion over the second momentum axis, which serves to relax the above idealized arguments. Nevertheless, it is *not* coincidental that the FS has the same (albeit weak) nesting vector, but a consequence of the expansion of the transitions about this energy.

This interpretation is consistent with the temperature dependence of the ARPES spectral function, which becomes gapped (by ~ 35 meV) in the commensurate CDW phase below 90 K.^{7,11,13,31} The gapping of the FS occurs most strongly on the K barrels, which completely disappear, as well as on the long sections of the M dogbone FS (e.g. the dogbone crossings along the KM direction). These are precisely the parts of the FS that were implicated in Fig. 4(c) as being involved in the finite energy

deep nesting.

To summarize, we have *experimentally* shown that the electronic instability at the FS is not sufficient to drive CDW order in $2H$ -TaSe₂. Instead, mechanisms that do not rely on details of the FS are more likely candidates for driving CDW order. For example, recent models include the wave vector dependence of the electron-phonon coupling,^{5,30} the condensation of preformed excitons,¹⁶ or strong electron-lattice coupling.³² The importance of analyzing the \mathbf{k} -dependence of the susceptibility function, at a suitable peak in \mathbf{q} -space, is clearly reflected in our ability to confidently identify *which* electronic states contribute to the susceptibility at the ordering wavevector. For example, previous experimental studies, which were based on either the autocorrelation,¹³ or a TB fit,¹⁹ of the ARPES FS (rather than analyzing a large energy range), concluded that FS nesting was important in driving the CDW of TaSe₂. In contrast, the analysis of the \mathbf{k} -dependence enables us to firmly rule this out, despite the similarity of our \mathbf{k} -integrated function to that of Ref. 19, bringing a much-needed consensus between ARPES experiment and theory.

V. MONOLAYER TaSe₂

Finally, we consider the situation in the absence of bilayer splitting through calculations of monolayer TaSe₂. In the monolayer, the interband transitions that were identified in the previous discussion of bulk TaSe₂ are not available, and instead just a single band contributes to the near- E_F electronic structure. Moreover, this system is truly 2D, containing no out-of-plane dispersion, and is therefore more fragile against instabilities in its FS.

Theoretically, the monolayer is modelled as a single TaSe₂ layer (with the same crystal parameters as the bulk) separated by a vacuum layer of ~ 20 Å, and the *ab initio* electronic structure is calculated using the FLAPW ELK code. No attempt has been made to relax the structural parameters. The FS of monolayer TaSe₂ is shown in Fig. 5(a), and consists of a rounded hexagon centered at Γ and a rounded triangle at K , similar in topology to previous results on monolayer TaSe₂¹⁷ and monolayer

NbSe₂.⁵ In Fig. 5(b), the susceptibility of this band structure is shown (and is in good agreement with previous calculations).¹⁷ The real part exhibits a strong peak centered close to $\frac{2}{3} \Gamma M$, although, similar to the bulk, the peak in the imaginary part remains broad and smaller than at $\mathbf{q} = K$. In (relaxed) monolayer NbSe₂, the peak in the susceptibility was found to shift to $\frac{1}{2} \Gamma M$.⁵

The \mathbf{k} -resolved susceptibility is shown in Fig. 5(c) for $\mathbf{q} = \frac{2}{3} \Gamma M$. In the absence of interband transitions, the peak in the susceptibility of the monolayer is associated with the saddle points of the band structure, which connect to the vicinity of the K FS sheet. This situation is reminiscent, although quantitatively different, to the saddle point nesting model, which was based on a single NbSe₂ band.¹⁴ Indeed, a more recent ARPES study postulated that both the saddle band and the K FS may be involved.¹¹ The peaks in both bulk and monolayer susceptibilities involve states near the saddle band region and near the K FS barrels, and it is this \mathbf{q} -vector that is most relevant in determining the susceptibility peak. However, the \mathbf{k} -dependence of the susceptibility is quite different in the monolayer, being restricted to narrow strips near the saddle band region. These results demonstrate the sensitivity of the \mathbf{k} -resolved susceptibility to changes in the active states at a particular \mathbf{q} -vector, and illustrate its value in assessing the origin of instabilities in the electronic subsystem.

VI. CONCLUSION

The connection between the FS and the CDW has been revisited in $2H$ -TaSe₂ through ARPES measurements.

After developing an accurate tight-binding model of the experimental electronic structure, the experimental susceptibility was calculated, and compared with *ab initio* calculations. Through careful analysis of the empirical \mathbf{k} -resolved electronic susceptibility function, finite energy transitions have been shown to dominate the susceptibility both at its peak, and at the CDW wave vector. This approach directly illustrates *which* states are involved in features of the electronic susceptibility. Whilst the conventional FS nesting model is considered too weak to drive the CDW, the FS is indirectly involved in determining the peak in the susceptibility, although the final choice of ordering vector likely depends on the lattice. Finally, comparison with theoretical calculations of 2D monolayer TaSe₂ illustrate the different electron states that are involved in the absence of bilayer splitting.

Acknowledgements

We would like to thank S. B. Dugdale and A. R. H. Preston for valuable discussions. The Boston University program is supported in part by the Department of Energy under Grant No. DE-FG02-98ER45680. The work in the UK was supported by EPSRC, UK, (EP/I007210/1) and the Boston University/University of Warwick collaboration fund. EA acknowledges support from Fundação para a Ciência e a Tecnologia, Portugal, through a doctoral degree fellowship (SFRH/BD/47847/2008).

-
- ¹ J. A. Wilson and A. D. Yoffe, *Adv. Phys.* **18**, 193 (1969).
² G. Grüner, *Density Waves in Solids* (Addison-Wesley, Reading, PA, 1994).
³ M.-H. Whangbo, E. Canadell, P. Foury and J.-P. Pouget, *Science* **252**, 96 (1991).
⁴ M. D. Johannes and I. I. Mazin, *Phys. Rev. B* **77**, 165135 (2008).
⁵ M. Calandra, I. I. Mazin and F. Mauri, *Phys. Rev. B* **80**, 241108(R) (2009).
⁶ K. Rossnagel, *J. Phys.: Condens. Matter* **23**, 213001 (2011).
⁷ R. Liu, C. G. Olson, W. C. Tonjes and R. F. Frindt, *Phys. Rev. Lett.* **80**, 5762 (1998).
⁸ T. Valla, A. V. Fedorov, P. D. Johnson, J. Xue, K. E. Smith and F. J. DiSalvo, *Phys. Rev. Lett.* **85**, 4759 (2000); T. Valla, A. V. Fedorov, P. D. Johnson, P.-A. Glans, C. McGuinness, K. E. Smith, E. Y. Andrei and H. Berger, *Phys. Rev. Lett.* **92**, 086401 (2004).
⁹ R. Liu, W. C. Tonjes, V. A. Greanya, C. G. Olson and R. F. Frindt, *Phys. Rev. B* **61**, 5212 (2000).
¹⁰ Th. Straub, Th. Finteis, R. Claessen, P. Steiner, S. Hüfner, P. Blaha, C. S. Oglesby and E. Bucher, *Phys. Rev. Lett.* **82**, 4504 (1999).
¹¹ W. C. Tonjes, V. A. Greanya, R. Liu, C. G. Olson and P. Molinié, *Phys. Rev. B* **63**, 235101 (2001).
¹² K. Rossnagel, E. Rotenberg, H. Koh, N. V. Smith and L. Kipp, *Phys. Rev. B* **72**, 121103(R) (2005).
¹³ S. V. Borisenko, A. A. Kordyuk, A. N. Yaresko, V. B. Zabolotnyy, D. S. Inosov, R. Schuster, B. Büchner, R. Weber, R. Follath, L. Patthey and H. Berger, *Phys. Rev. Lett.* **100**, 196402 (2008).
¹⁴ T. M. Rice and G. K. Scott, *Phys. Rev. Lett.* **35**, 120 (1975).
¹⁵ R. L. Barnett, A. Polkovnikov, E. Demler, W.-G. Yin and W. Ku, *Phys. Rev. Lett.* **96**, 026406 (2006).
¹⁶ A. Taraphder, S. Koley, N. S. Vidhyadhiraja and M. S. Laad, *Phys. Rev. Lett.* **106**, 236405 (2011).
¹⁷ Y. Ge and A. Y. Liu, *Phys. Rev. B* **86**, 104101 (2012).
¹⁸ D. E. Moncton, J. D. Axe and F. J. DiSalvo, *Phys. Rev. Lett.* **34**, 734 (1975).
¹⁹ D. S. Inosov, V. B. Zabolotnyy, D. V. Evtushinsky, A. A. Kordyuk, B. Büchner, R. Follath, H. Berger and S. V. Borisenko, *New J. Phys.* **10**, 125027 (2008).
²⁰ J. K. Dewhurst, S. Sharma, L. Nordstöm, F. Cricchio, F. Bultmark and E. K. U. Gross, <http://elk.sourceforge.net> (2012).

- ²¹ D. E. Moncton, J. D. Axe and F. J. DiSalvo, *Phys. Rev. B* **16**, 801 (1977).
- ²² K. Rossnagel and N. V. Smith, *Phys. Rev. B* **76**, 073102 (2007).
- ²³ G. Wexler and A. M. Woolley, *J. Phys. C: Solid State Phys.* **9**, 1185 (1976).
- ²⁴ M. Naito and S. Tanaka, *J. Phys. Soc. Jpn.* **51**, 219 (1982); E. Revolinsky, B. E. Brown, D. J. Beerntsen and C. H. Armitage, *J. Less-Common Met.* **8**, 63 (1965).
- ²⁵ P. Zhang, P. Richard, T. Qian, Y.-M. Xu and X. Dai, *Rev. Sci. Instrum.* **82**, 043712 (2011).
- ²⁶ F. James, CERN Program Library D506, MINUIT—Function Minimization and Error Analysis, 1994, <http://consult.cern.ch/writeups/minuit>, <http://c-minuit.sourceforge.net>.
- ²⁷ Taking i as the index into the ordered set, $|\mathbf{R}|$, the $E_{0,j}$ where j is the band index, and $t_{i,j}$ ($1 \leq i \leq 15$), are (in meV): $E_{0,1} = -79.4$; $t_{i,1} = 20.5, 74.1, -12.0, -2.9, -3.1, -0.1, 0.3, 4.2, 2.5, 3.1, 3.3, 5.1, 2.8, 0.6, 2.3$; $E_{0,2} = 118.1$; $t_{i,2} = 35.9, 91.6, -3.6, 6.5, -8.7, 2.9, 5.8, -11.9, -5.0, 5.3, -3.5, -1.0, -0.4, 1.5, -0.3$.
- ²⁸ J. Laverock, T. D. Haynes, C. Uffeld and S. B. Dugdale, *Phys. Rev. B* **80**, 125111 (2009).
- ²⁹ M. D. Johannes, I. I. Mazin and C. A. Howells, *Phys. Rev. B* **73**, 205102 (2006).
- ³⁰ F. Weber, S. Rosenkranz, J.-P. Castellan, R. Osborn, R. Hott, R. Heid, K.-P. Bohnen, T. Egami, A. H. Said and D. Reznik, *Phys. Rev. Lett.* **107**, 107403 (2011).
- ³¹ J. Demsar, L. Forró, H. Berger and D. Mihailovic, *Phys. Rev. B* **66**, 041101(R) (2002).
- ³² L. P. Gor'kov, *Phys. Rev. B* **85**, 165142 (2012).